

Unit-Based Histopathology Tissue Segmentation via Multi-Level Feature Representation

Ashkan Shakarami^{1*}, Azade Farshad², Yousef Yeganeh², Lorenzo Nicolè¹,
Peter Schüffler², Stefano Ghidoni¹, Nassir Navab²

¹University of Padova, Italy

²Technical University of Munich, Germany

ashkan.shakarami@phd.unipd.it, lorenzo.nicole@phd.unipd.it, stefano.ghidoni@unipd.it,
azade.farshad@tum.de, y.yeganeh@tum.de, peter.schueffler@tum.de, nassir.navab@tum.de

Abstract

We propose **UTS**, a unit-based tissue segmentation framework for histopathology that classifies each fixed-size 32×32 tile, rather than each pixel, as the segmentation unit. This approach reduces annotation effort and improves computational efficiency without compromising accuracy. To implement this approach, we introduce a Multi-Level Vision Transformer (L-ViT), which benefits the multi-level feature representation to capture both fine-grained morphology and global tissue context. Trained to segment breast tissue into three categories (*infiltrating tumor*, *non-neoplastic stroma*, and *fat*), UTS supports clinically relevant tasks such as tumor-stroma quantification and surgical margin assessment. Evaluated on 386,371 tiles from 459 H&E-stained regions, it outperforms U-Net variants and transformer-based baselines. Code and Dataset will be available at GitHub.

Keywords: Unit-Based Segmentation, Histopathology, Vision Transformers, Multi-Level Feature Representation.

1 Introduction

Accurate tissue segmentation in histopathological Whole Slide Images (WSIs) is fundamental to digital pathology, enabling computational support for diagnosis, prognosis, and treatment planning [1–3]. Conventional approaches, such as U-Net [4] and DeepLab [5], rely on pixel-wise segmentation, which requires dense annotations, is prone to noisy

outputs, and incurs substantial computational costs—especially at gigapixel resolution [6, 7].

Transformer-based architectures such as TransUNet [8], Swin-UNet [9], and H2G-Net [10] have enhanced global context modeling and multiscale feature learning (A literature review is provided in Appendix B, which discusses related work in more detail). However, they remain fundamentally tied to the pixel-wise paradigm, which limits scalability in clinical environments with hardware constraints.

We propose **UTS**, which treats each fixed-size 32×32 tile as a semantic unit rather than relying on conventional pixel-wise segmentation. This approach redefines the segmentation primitive to better align with how pathologists interpret tissue on WSI, and enables scalable analysis without the overhead of dense annotation. To operationalize this approach, we introduce **L-ViT**, a new Multi-Level Vision Transformer architecture designed to capture local and global histological patterns.

Unlike pixel-wise segmentation at down-sampled resolutions, which averages tissue information across regions, UTS retains high-resolution morphological detail within each 32×32 tile (subsection 3.5).

L-ViT incorporates an EfficientNetB3 backbone and fuses multi-scale features through Multi-Level Feature Fusion (MLFF) for hierarchical representation learning. Attention modules, including Dilated Attention and Squeeze-and-Excitation (DAT-SE) and Dilated Convolutional Block Attention Module (D-CBAM), further enhance spatial and channel-level discrimination. By decoupling segmentation from pixel-level granularity and

*Corresponding
ashkan.shakarami@phd.unipd.it

author:

enabling rich context modeling, UTS provides a computationally efficient, interpretable, and clinically aligned framework for whole-slide tissue analysis.

2 UTS

UTS, as illustrated in Figure 1, presents an end-to-end framework for histopathological tissue segmentation, encompassing Data acquisition, preprocessing (subsection 2.1), segmentation (subsection 2.2), and visualization (subsection 2.3). Appendix A also proves theoretical justification of UTS.

2.1 Data Acquisition and Preprocessing

UTS begins with the acquisition of H&E-stained WSIs, digitized from tissue samples obtained through biopsy or surgical resection. To prepare these high-resolution WSIs for segmentation, we employ the SlideTiler toolbox [11], which facilitates efficient and standardized preprocessing.

In this stage, a pathologist selects either ROIs or entire slide areas. SlideTiler then partitions these selections into uniform 32×32 pixel tiles. Formally, each WSI or ROI I_i is divided into N tiles T_{ij} , i.e., $I_i = \bigcup_{j=1}^N T_{ij}$, where each tile (semantic unit) T_{ij} is stored in PNG format.

Unlike traditional tools such as QuPath, SlideTiler automates tile generation and preserves diagnostically relevant structures while excluding background and artifacts. This standardized tile-based format reduces preprocessing overhead and aligns with the unit-based segmentation approach of UTS, allowing for seamless downstream processing by the L-ViT segmentation engine (subsection 2.2). The resulting tiles serve as input to the classification model, forming a scalable and annotation-efficient representation of histological content. This tile-level granularity reflects how pathologists often interpret morphology in discrete regions, enabling efficient and interpretable segmentation aligned with clinical workflow.

2.2 Segmentation

The core segmentation engine of UTS classifies each 32×32 tile into one of three histologi-

cal classes: *infiltrating tumor*, *non-neoplastic stroma*, or *fat*. This classification approach is powered by L-ViT (detailed in subsection 2.2.1), a vision transformer architecture adapted for histopathological tile segmentation. The model receives raw image tiles and outputs class probabilities directly, without requiring postprocessing or pixel-level masks. This simplifies annotation, reduces computational overhead, and aligns with how pathologists reason about tissue morphology at the regional level. By integrating the segmentation output over the entire slide or ROI, UTS reconstructs a coarse-grained, semantically meaningful segmentation map that supports downstream clinical tasks such as tumor quantification and tissue composition analysis.

2.2.1 L-ViT

Figure 2 illustrates an overview of L-ViT. It adopts EfficientNetB3 as the backbone, taking advantage of its lightweight and efficient design, which offers high flexibility in adapting to varying input sizes and computational constraints through compound scaling [12, 13]. L-ViT also integrates the DAT-SE for channel-wise feature recalibration (section 2.2.1) [14] and D-CBAM to apply channel and spatial attention (section 2.2.1) [15]. In addition, MLFF [16, 17] ensures effective integration of features at different stages of the network. L-ViT incorporates Transformer blocks in its final layers to capture long-range dependencies [18], as well. The refined feature maps are processed through dense layers, culminating in a softmax layer for multi-class classification. The following subsections provide further details on each component.

DAT-SE. DAT-SE enhances feature representation by applying channel-wise and spatial attention mechanisms, dynamically recalibrating input feature maps to improve their discriminative power [14]. Given an input feature map $\mathbf{X} \in \mathbb{R}^{H \times W \times C}$, channel attention is computed by extracting global context information through Global Average Pooling (GAP), transforming the feature map into a channel descriptor $\mathbf{z} \in \mathbb{R}^C$. This representation is processed through two fully connected layers, followed by a sigmoid activation to generate channel-wise attention weights:

$$\mathbf{s} = \sigma(\mathbf{W}_2 \delta(\mathbf{W}_1 \mathbf{z})). \quad (1)$$

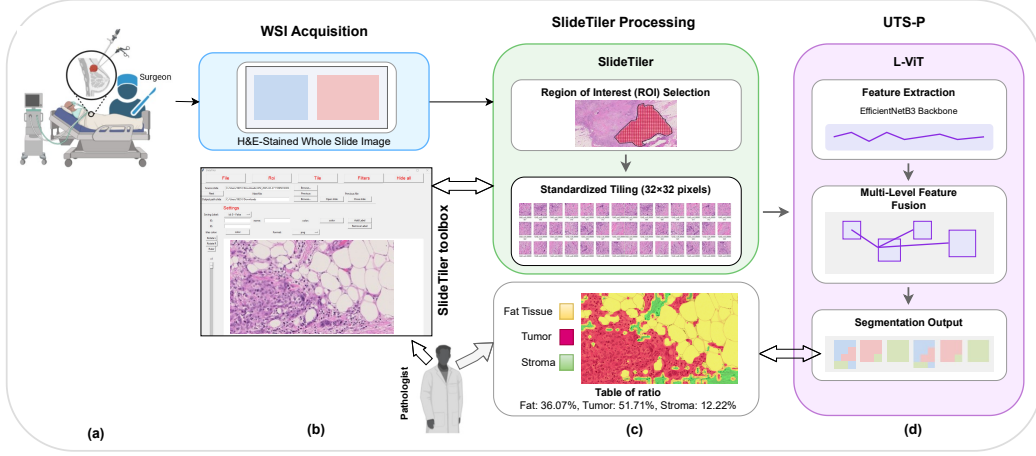


Figure 1: **UTS Pipeline.** (a) Tissue extraction via biopsy or surgery. (b) H&E-stained WSI acquisition through processing, staining, and digitization. (c) SlideTiler preprocessing for WSI or ROI selection and standardized tiling into 32×32 pixel tiles. (d) Segmentation using L-ViT to classify tiles into *Infiltrating Breast Tumor*, *Fat Tissue*, and *Non-neoplastic Stroma*, visualized with color-coded overlays. The system also computes tissue composition ratios (e.g., Tumor: 51.71%, Stroma: 12.22%, Fat: 36.07%), enabling automated tumor-stroma quantification based on unit-level classification using fixed-size 32×32 tiles. This integrated analysis supports Tumor-Stroma Ratio (TSR) estimation, providing interpretable metrics for prognostic assessment and personalized treatment planning.

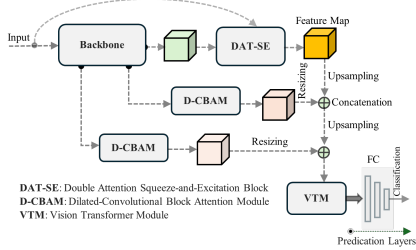


Figure 2: Overview of L-ViT. MLFF integrates low-, mid-, and high-level features to enhance classification accuracy by combining local and global context. For component details, refer to DAT-SE (section 2.2.1), D-CBAM (section 2.2.1), and VTM (section 2.2.1).

Simultaneously, spatial attention enhances spatial feature relationships by capturing contextual dependencies. This is achieved through average and max pooling across the channel dimension, followed by a convolutional layer to generate spatial attention weights:

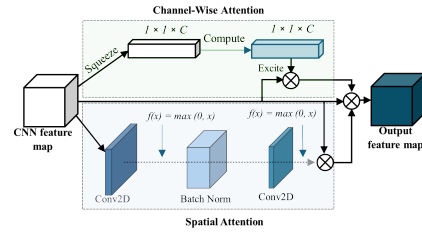


Figure 3: DAT-SE (section 2.2.1): Enhances feature representation by recalibrating input maps with channel and spatial attention [14].

$$\mathbf{M}_{\text{spatial}} = \sigma(\text{conv}([\text{avg}(\mathbf{X}); \text{max}(\mathbf{X})])). \quad (2)$$

The final feature recalibration integrates both attention mechanisms, refining feature representation as:

$$\mathbf{X}' = \mathbf{X} \cdot \mathbf{s} \cdot \mathbf{M}_{\text{spatial}}. \quad (3)$$

This dual-attention mechanism amplifies relevant features while suppressing irrelevant information, enhancing segmentation accuracy and robustness in histopathological image analysis.

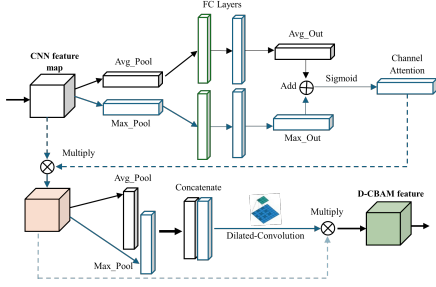


Figure 4: D-CBAM (section 2.2.1): Extends CBAM [15,19] by integrating channel and spatial attention for improved feature focus.

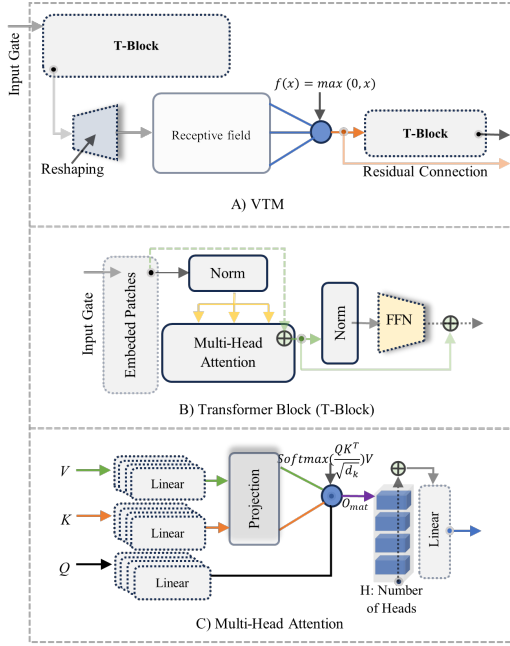


Figure 5: VTM Architecture (section 2.2.1), utilizing Transformer blocks [18] with Multi-Head Self-Attention, Feed-Forward Networks, and Layer Normalization.

D-CBAM. D-CBAM is an improved Channel and Spatial Attention Mechanism inspired by CBAM [15,19]. It enhances feature selection by integrating dilated convolutions and refining long-range feature dependencies while preserving fine-grained spatial details. Channel attention aggregates contextual information across channels using GAP and Global Max Pooling (GMP). These pooled features are then passed through fully connected layers, followed by sigmoid activation, to obtain channel-wise attention weights, formulated as $\mathbf{M}_c = \sigma(\mathbf{W}_0(\delta(\mathbf{W}_1(\text{GAP}(\mathbf{X}))) + \delta(\mathbf{W}_1(\text{GMP}(\mathbf{X}))))$. Spatial attention en-

hances spatial feature representation by applying dilated convolutions over concatenated average and max pooled feature maps as Equation 4.

$$\mathbf{M}_s = \sigma(\text{conv}_{\text{dilated}}([\text{avgpool}(\mathbf{X}); \text{maxpool}(\mathbf{X})])). \quad (4)$$

The final refined feature map is computed as Equation 5. D-CBAM effectively expands the receptive field by incorporating dilated convolutions, improving segmentation effectiveness by capturing local fine-grained and global structural information.

$$\mathbf{X}' = \mathbf{X} \cdot \mathbf{M}_c \cdot \mathbf{M}_s. \quad (5)$$

VTM. VTM integrates Transformer blocks [18] to model long-range dependencies and improve contextual understanding in histopathological tissue analysis. Figure 5 shows VTM with Transformer blocks (T-Block). Within each T-Block, the Multi-Head Self-Attention (MHSA) mechanism computes attention weights by processing the query, key, and value matrices, where each attention head is defined as $\text{head}_i = \text{softmax}\left(\frac{Q_i K_i^T}{\sqrt{d_k}}\right) V_i$. The outputs from multiple heads are then concatenated to form the final multi-head attention output, formulated as $\text{MHSA}(Q, K, V) = \text{concat}(\text{head}_1, \dots, \text{head}_h) W_O$. Following MHSA, a FFN further refines feature representations through a two-layer transformation with ReLU activation, given by $\text{FFN}(X) = \text{ReLU}(XW_1 + b_1)W_2 + b_2$. To ensure stable training and effective feature transformation, Layer Normalization, and Residual Connections are applied, where the final normalized output is computed as $Y_{\text{norm}} = \text{LayerNorm}(X + \text{MHSA}(Q, K, V) + \text{FFN}(X))$. Moreover, VTM incorporates Multi-Head Linear Attention [20]. This Linear Attention reduces the complexity from quadratic to linear with respect to the sequence length. This is achieved by projecting the query and key matrices into a lower-dimensional space, formulated as $Q' = QW_Q$, $K' = KW_K$.

2.3 Visualization

The segmentation output obtained from the UTS framework exhibits a tile-wise structure. As a result, edge boundaries are observed,

which affects the spatial coherence of the segmented regions. Hence, we use the *Segmentation Refinement* as a post-processing strategy with no additional computational cost (section 2.3), integrated end-to-end with L-ViT, to refine the final segmentation output and address this issue. This strategy uses Neighborhood-Based Smoothing and Class Discretization, as explained below.

The refinement method consisted of two main stages: (i) a local smoothing operation using a separable filter to mitigate abrupt transitions between neighboring tiles and (ii) a class discretization step to enforce categorical consistency across the refined segmentation mask.

Neighborhood-Based Smoothing: A separable filtering approach was employed to refine the segmentation mask and enhance boundary consistency. This method computes the local mean of pixel values within a defined neighborhood of size 48×48 pixels, corresponding to 1.5 times the tile size. Separable filtering decomposes the operation into two successive one-dimensional convolutions with a linear complexity ($O(2k)$, where k denotes the neighborhood radius). The refined segmentation mask $S_f(x, y)$ at a given pixel location (x, y) was computed in two sequential steps:

1. Horizontal Filtering: A one-dimensional convolution is first applied along the horizontal axis to smooth pixel intensities within a fixed neighborhood:

$$S'_f(x, y) = \frac{1}{N} \sum_{i=-k}^k S(x + i, y), \quad (6)$$

2. Vertical Filtering: The intermediate result is then processed along the vertical axis to obtain the final refined segmentation mask:

$$S_f(x, y) = \frac{1}{N} \sum_{j=-k}^k S'_f(x, y + j), \quad (7)$$

where $S(x, y)$ represents the original segmentation mask, k denotes the neighborhood radius, and N is the total number of pixels within the local region. This method achieves a substantial computational speedup by leveraging separable filtering while preserving segmentation precision, making it particularly suitable for large-scale histopathological image analysis.

Class Discretization: Since the smoothing operation may introduce intermediate values deviating from the predefined class labels (absolute values for Red, Green, and Yellow representing Infiltrating Breast Tumors, Fat Tissue, and Non-neoplastic Stroma), a refinement step was applied to discretize the filtered output into distinct categories. Each pixel in the smoothed image was mapped to the closest predefined class by minimizing the Euclidean distance between its intensity vector and the corresponding class color centroid in the RGB space:

$$C(x, y) = \arg \min_{c \in \{R, G, Y\}} \|S_f(x, y) - C_c\|_2, \quad (8)$$

where C_c represents the class-specific color values for tumor (red: [255, 0, 0]), stroma (green: [0, 255, 0]), and fat (yellow: [255, 255, 0]). This step ensured the segmentation output remained interpretable, avoiding unsmooth edges introduced by continuous-valued tile-based filtering.

WSI Overlay: Segmentation outputs should align with pathologists' diagnostic workflow to support clinical decision-making [13, 21–24]. To support this, UTS generates segmentation overlays that integrate with histological slides, preserving tissue morphology as shown in Figure 6. This enables direct validation of the method's predictions without disrupting standard diagnostic practices. UTS's visual outputs can function as an assistive tool rather than a replacement for expert judgment, allowing for direct comparison with histological evidence.

To visualize the refined segmentation within the context of the original histopathological slide, the final segmentation mask is applied to the original WSI using a weighted overlay technique:

$$I_{overlay} = \alpha S_d + (1 - \alpha) I_{WSI}, \quad (9)$$

where S_d denotes the discretized segmentation, I_{WSI} represents the original WSI, and α is a transparency coefficient ($\alpha = 0.5$). This visualization approach maintained the tissue morphology while clearly delineating the segmented regions.

Refinement Computational Complexity: The computational complexity of the segmentation refinement method is given by $O(2k + 4)$,

where $O(2k)$ arises from the separable filtering process (section 2.3), which consists of two successive 1D convolutions (horizontal and vertical). $O(3)$ corresponds to the class discretization step, where each pixel’s RGB value is compared against the three predefined class colors. $O(1)$ accounts for the WSI overlay, which applies a simple linear blending operation per pixel. Since k (the neighborhood radius) is larger than the constant terms, the overall computational complexity can be approximated as $O(k)$, making the method highly efficient for large-scale histopathological image analysis.

In addition, the additional complexity above introduced by the segmentation refinement method, $O(k)$, is significantly lower than the existing complexities of the models in Table 5. Since the primary computational load in L-ViT arises from tokenized tile-based segmentation, given by $O(M^2 \cdot D/k^2)$, adding a post-processing step with $O(k)$ complexity does not substantially impact the overall model complexity, as it is asymptotically negligible in comparison to $O(M^2 \cdot D/k^2)$. Therefore, the overall computational complexity of L-ViT (Table 5) remains unchanged, and the dominant complexity term remains as Equation 10.

$$O(M^2 \cdot D/k^2) + O(k) = O(M^2 \cdot D/k^2). \quad (10)$$

Results and Impact: The refinement method improved segmentation smoothness and boundary continuity without compromising class accuracy. By integrating neighborhood-based filtering and class discretization, it effectively reduced tile-induced artifacts and enhanced clinical interpretability. As shown in Figure 6, subfigure (a) displays the original ROI, and (b) shows the raw tile-based segmentation output with visible blockiness. Subfigure (c) overlays the refined segmentation onto the ROI, highlighting improved spatial consistency, while (d) presents the final segmentation mask with smoother, more anatomically coherent class boundaries.

3 Experiments

3.1 Dataset

As shown in Table 1), the dataset comprises 459 ROIs, retrospectively selected from X

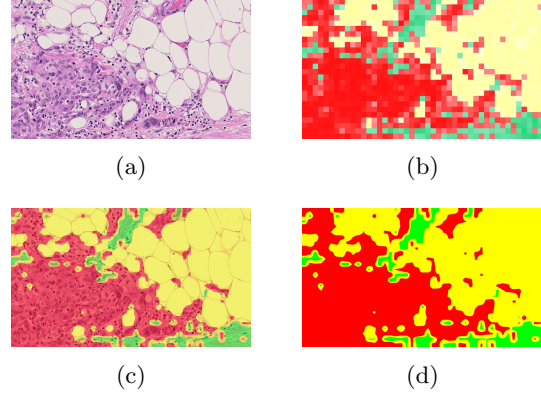


Figure 6: Visualization of segmentation refinement: (a) Original ROI from H&E-stained tissue, (b) unrefined segmentation output from tile classification, (c) refined segmentation overlaid on the original ROI, and (d) final refined segmentation. Red, Yellow, and Green indicate *Infiltrating Breast Tumors*, *Fat Tissue*, and *Non-neoplastic Stroma*, respectively.

Table 1: Dataset information (Number of Tiles and Samples per Category)

Categories	Tiles	ROIs
Fat Tissue	100221	153
Non-neoplastic Stroma	160067	153
Infiltrating Breast Tumors	126083	153
Total	386371	459

anonymized H&E-stained WSIs acquired at 20× magnification using the Ventana DP200 scanner. Each ROI was annotated by a board-certified pathologist to represent a single histological category—either *Infiltrating Breast Tumor*, *Non-neoplastic Stroma*, or *Fat Tissue*—ensuring **purity** of class content within each ROI. These ROIs were then processed using SlideTiler [11], which partitions them into standardized 32×32 pixel tiles. In total, 386,371 tiles were generated, distributed as follows: 100,221 fat tiles, 160,067 stroma tiles, and 126,083 tumor tiles. This class-pure ROI design eliminates ambiguous boundaries, simplifies annotation, and strengthens the reliability of class-specific learning during training. The size of the selected ROIs was between X and Y pixels.

3.2 Performance

All reported performance metrics are computed as **macro-averages** across the three tissue classes to ensure equal contribution

from each category, regardless of class imbalance.

UTS outperformed baseline CNNs (MobileNetV2 [25], ResNet50 [26], and EfficientNet-B3 [12]) as well as state-of-the-art models such as Attention U-Net [27], ResUNet++ [28], and H2G-Net [29], as shown in Table 2 and Table 3. A 3-fold patient-level cross-validation ensured robust evaluation and avoided data leakage.

Compared to MobileNetV2 (IoU: $72.68 \pm 6.43\%$, DSC: $83.76 \pm 4.92\%$), UTS achieved $84.44 \pm 1.89\%$ IoU and $91.37 \pm 1.64\%$ DSC, reflecting gains of 11.76% and 7.61%, respectively. Against ResNet50 (IoU: $80.25 \pm 3.06\%$, DSC: $88.95 \pm 2.74\%$), improvements of 4.19% in IoU and 2.42% in DSC were observed. With approximately 128,790 tiles per validation fold (Table 1), each 1% improvement translates to over 1,200 additional correctly segmented tiles—highlighting the clinical relevance of even marginal gains.

Although L-ViT yielded the best results, one of UTS’s notable advantages is its architectural flexibility. CNNs like ResNet50 still achieved high performance within the unit-based segmentation pipeline, benefiting from the structured tile-level approach. This demonstrates that UTS is a robust host framework adaptable to both lightweight and high-capacity models, enabling deployment across a range of clinical and hardware environments.

Table 2: Comparison of L-ViT with CNNs within UTS framework

Model	Acc	R	Spec	DSC	IoU
MobileNetV2 [25]	84.76	81.60	90.36	83.76	72.68
ResNet50 [26]	88.79	89.27	93.83	88.95	80.25
EfficientNet-B3 [12]	89.98	89.41	94.15	89.91	81.74
L-ViT	90.92	91.06	95.10	91.37	84.44

Beyond CNN-based models, UTS was benchmarked against advanced architectures such as Attention U-Net, ResUNet++, H2G-Net, and BEFUnet. BEFUnet, the most competitive state-of-the-art model, achieved an IoU of 77.60% and DSC of 87.10% (Table 3). However, UTS outperformed all models, achieving the highest DSC (91.37%) and IoU (84.44%). These improvements demonstrate UTS’s superior capability in differentiating between histological components, including Infiltrating Breast Tumor, Fat Tissue, and Non-neoplastic Stroma regions.

Table 3: Comparison of UTS with State-of-the-Art Models

Model	Acc	R	P	DSC	IoU
Attention U-Net [27]	-	84.00	82.50	-	-
ResUNet++ [28]	-	70.22	87.85	-	79.62
H2G-Net [29]	-	87.90	90.70	-	-
BEFUnet [30]	87.03	90.80	87.30	87.10	77.60
UTS (Ours)	90.92	91.06	91.68	91.37	84.44

3.3 Ablation Study

To evaluate the contributions of individual components in our proposed **L-ViT** architecture, we conducted an ablation study by incrementally incorporating key modules and analyzing their effects on segmentation performance. Table 4 summarizes the results of different architectural configurations in terms of DSC, Recall, IoU, Accuracy, and Specificity.

Baseline Model. The baseline model utilizes EfficientNet-B3 as the backbone without additional enhancement modules. As shown in Table 4, this configuration achieves a DSC of 89.91 ± 0.54 , an IoU of 81.74 ± 0.75 , and an accuracy of $89.98 \pm 0.56\%$. While EfficientNet-B3 provides strong feature extraction, it lacks advanced spatial and attention-based feature refinement, which limits overall segmentation accuracy.

Effect of VTM. Integrating the VTM with EfficientNet-B3 improves performance across all metrics. The DSC increases to 90.67, and IoU improves to 83.36, indicating that the VTM effectively captures long-range dependencies and enhances feature representation. This demonstrates that replacing purely convolutional feature extraction with transformer-based modeling yields better segmentation outcomes. As previously noted, even slight performance improvements can noticeably enhance segmentation performance. For instance, a 1% increase in segmentation performance translates to 1287 additional correctly segmented tiles during evaluation (Given the scale of our dataset (Table 1), with approximately 128790 tiles per validation fold, such gains can have a substantial impact).

Contribution of DAT-SE. Further incorporating DAT-SE alongside VTM enhances feature recalibration by dynamically adjusting channel-wise importance. This further in-

creases DSC (90.85) and IoU (83.63), with recall reaching 91.16%.

Impact of MLFF and D-CBAM. By jointly incorporating MLFF and D-CBAM, L-ViT reaches the highest segmentation performance: DSC: 91.37 ± 1.13 , IoU: 84.44 ± 1.89 , and Accuracy: 90.92 ± 1.14 . These improvements confirm that MLFF effectively enhances information propagation across different feature levels, while D-CBAM refines spatially important regions, leading to a more robust segmentation performance.

Table 4: Ablation study results for different L-ViT components.

Component	DSC	R	IoU	Acc	Spec
Backbone	89.91	89.41	81.74	89.98	94.15
+ VTM	90.67	91.11	83.36	90.68	95.00
+ VTM & DAT-SE	90.85	91.16	83.63	90.68	95.05
All (L-ViT)	91.37	91.06	84.44	90.92	95.10

As the final observation, the ablation study confirms that each component in L-ViT contributes to segmentation quality. The backbone (EfficientNet-B3) provides strong initial feature extraction, VTM introduces global attention, DAT-SE refines feature representation, MLFF ensures hierarchical feature integration, and D-CBAM further improves spatial attention.

3.4 Efficiency and Advantages

Traditional pixel-wise segmentation in WSI analysis requires up to $N = 512 \times 512 = 262,144$ operations per patch, making it computationally intensive. In contrast, UTS reduces the burden by processing only 256 non-overlapping tiles per image when using 32×32 units—yielding a 1024-fold reduction in operations per patch while maintaining segmentation accuracy.

Compared to CNN-based architectures such as U-Net [4], with complexity $\mathcal{O}(N \cdot K^2 \cdot C_{in} \cdot C_{out})$, UTS benefits from a simplified input structure and a more scalable processing path. The use of tokenized inputs and multi-level fusion in L-ViT reduces computational complexity to $\mathcal{O}(M^2 \cdot D/k^2)$, where k is the tile size. The lightweight refinement step, discussed in subsection 2.3, adds only linear-time complexity $\mathcal{O}(k)$ and does not affect overall scalability. This efficiency translates well to real-world conditions. We benchmarked UTS

on a single NVIDIA GeForce RTX 3060 GPU with an Intel® Core™ i7-11800U CPU and 16 GB RAM. Training required only 90 seconds per epoch (batch size 64), demonstrating the framework’s compatibility with modest hardware resources [31, 32].

Table 5: Computational Complexity Comparison

Model	Complexity	Approach
U-Net [4]	$\mathcal{O}(N \cdot K^2 \cdot C_{in} \cdot C_{out})$	Pixel-wise
HIPT [21]	$\mathcal{O}(M^2 \cdot D)$	Patch-based
UTS	$\mathcal{O}(M^2 \cdot D/k^2)$, k : tile dimension	Unit-based

In addition to efficiency, UTS offers practical advantages through its design. The integration of MLFF consolidates low- and high-level features, enhancing robustness across heterogeneous histological regions. Coupled with the EfficientNet-B3 backbone, this enables context-aware segmentation that balances resolution and generalizability. UTS also supports interpretability by producing decision maps and probability-based heatmaps that can be directly overlaid onto WSIs, an essential feature for diagnostic workflows involving uncertainty and tissue complexity.

3.5 $1\times$ vs. $20\times$ Resolution

Although segmentation via classification is not novel per se, UTS offers a key advantage by operating on full-resolution 32×32 tiles, which preserve fine-grained morphological features essential for histopathological analysis. In contrast, a pixel-wise segmentation model applied to $1\times$ downsampled WSIs would treat each pixel as representing an entire 32×32 patch from the original resolution. This downsampling process effectively averages information over those regions, resulting in the loss of fine structural details such as nuclear boundaries, gland formations, or stromal texture.

Therefore, while a $1\times$ pixel-wise segmentation may seem equivalent in spatial scale to unit-based classification, it lacks access to the high-resolution content. UTS, by classifying tiles in the standard resolution ($20\times$), retains diagnostic features that are crucial for accurate tissue discrimination. This theoretical advantage aligns with pathologists’ reliance on high-resolution morphology and supports UTS’s superior performance in segmenting tumor, stroma, and fat tissue with high fidelity.

4 Limitations and Future Work

While UTS demonstrates strong segmentation performance, several limitations remain. Blank or non-informative regions in WSIs, such as background or slide borders that do not belong to tumor, stroma, or fat classes, were excluded from the dataset to avoid label noise and inconsistent supervision. While this improves training stability, it limits direct generalization to whole slides with such regions, and future work may introduce an explicit null-class for handling them. Moreover, UTS currently employs a custom transformer trained from scratch; integrating foundation models like DINOv2 [33] could improve generalization and reduce training cost. The use of fixed 32×32 tiles also restricts compatibility with datasets such as CAMELYON16 [34], which require tiling standardization. In addition, MLFF uses fixed-weight fusion, which could be improved with adaptive strategies to better capture intra-slide variability. Finally, UTS may serve as a fast front-end module for coarse-to-fine pipelines [35].

Although UTS currently focuses on segmenting three primary breast tissue types (tumor, stroma, and fat), it can be readily extended to additional categories such as necrosis, lymphocytic infiltration, or benign epithelium, provided appropriate annotations. Moreover, while our experiments were conducted on expert-defined ROIs to ensure purity and class balance, UTS is architecturally compatible with whole-slide inference. Given its tile-based design and runtime efficiency (see subsection 3.4), full-slide segmentation is feasible through parallelized batch inference and will be investigated in future large-scale deployments.

5 Conclusion

We introduced **UTS-P**, a unit-based segmentation framework that redefines the segmentation primitive from pixels to tiles, enabling scalable and interpretable histopathological image analysis. Using a lightweight yet powerful architecture (**L-ViT**), integrating multi-level feature fusion, hierarchical attention modules, and a refinement strategy, UTS achieves high segmentation performance on clinically relevant breast tissue categories:

infiltrating tumor, non-neoplastic stroma, and fat. Our results demonstrate that unit-based segmentation can match or exceed the performance of state-of-the-art pixel-wise methods while offering improvements in computational efficiency, annotation cost, and visual interpretability. Furthermore, UTS’s compatibility with resource-constrained hardware makes it a practical solution for real-world clinical environments. We believe this approach opens new avenues for scalable, annotation-efficient, and diagnostically aligned segmentation systems in digital pathology and beyond.

References

- [1] G. Litjens, T. Kooi, B. E. Bejnordi, A. A. Setio, F. Ciompi, M. Ghafoorian, and J. A. van der Laak. A survey on deep learning in medical image analysis. *Medical Image Analysis*, 42:60–88, 2017.
- [2] T. Wan, L. Zhao, H. Feng, D. Li, C. Tong, and Z. Qin. Robust nuclei segmentation in histopathology using asppu-net and boundary refinement. *Neurocomputing*, 408:144–156, 2020.
- [3] A. Shakarami. Transformative ai for automating histopathology workflows. *Università degli studi di Padova*, 2025.
- [4] O. Ronneberger, P. Fischer, and T. Brox. U-net: Convolutional networks for biomedical image segmentation. In *Medical Image Computing and Computer-Assisted Intervention—MICCAI 2015*, pages 234–241. Springer, 2015.
- [5] L. C. Chen, G. Papandreou, I. Kokkinos, K. Murphy, and A. L. Yuille. Deeplab: Semantic image segmentation with deep convolutional nets, atrous convolution, and fully connected crfs. *IEEE Transactions on Pattern Analysis and Machine Intelligence*, 40(4):834–848, 2017.
- [6] S. Minaee, Y. Boykov, F. Porikli, A. Plaza, N. Kehtarnavaz, and D. Terzopoulos. Image segmentation using deep learning: A survey. *IEEE Transactions on Pattern Analysis and Machine Intelligence*, 44(7):3523–3542, 2021.
- [7] H. Xu, Q. Xu, F. Cong, J. Kang, C. Han, Z. Liu, and C. Lu. Vision transformers for computational histopathology. *IEEE Reviews in Biomedical Engineering*, 2023.
- [8] J. Chen, Y. Lu, Q. Yu, X. Luo, E. Adeli, Y. Wang, and L. Xing. Transunet: Transformers make strong encoders for medical image segmentation. *Medical Image Analysis*, 67:101848, 2021.

- [9] H. Cao, Y. Wang, J. Chen, D. Jiang, X. Zhang, Q. Tian, and M. Wang. Swin-unet: Unet-like pure transformer for medical image segmentation. *arXiv preprint*, 2021.
- [10] Y. Zhou, F. Yang, Z. Deng, H. Zhao, Y. Lu, and L. Xing. H2g-net: Hybrid hierarchical graph network for cell segmentation in histopathological images. *Medical Image Analysis*, 75:102283, 2022.
- [11] L. Barcellona, L. Nicolè, R. Cappellesso, A. P. Dei Tos, and S. Ghidoni. Slidetiler: A dataset creator software for boosting deep learning on histological whole slide images. *Journal of Pathology Informatics*, 15:100356, 2024.
- [12] M. Tan and Q. V. Le. Efficientnet: Rethinking model scaling for convolutional neural networks. In *Proceedings of the 36th International Conference on Machine Learning*, volume 97, pages 6105–6114, 2019.
- [13] A. Shakarami, L. Nicolè, M. Terreran, A. P. Dei Tos, and S. Ghidoni. Tcnn: A transformer convolutional neural network for artifact classification in whole slide images. *Biomedical Signal Processing and Control*, 84:104812, 2023.
- [14] J. Hu, L. Shen, and G. Sun. Squeeze-and-excitation networks. In *Proceedings of the IEEE Conference on Computer Vision and Pattern Recognition*, pages 7132–7141, 2018.
- [15] S. Woo, J. Park, J. Y. Lee, and I. S. Kweon. Cbam: Convolutional block attention module. In *Proceedings of the European Conference on Computer Vision (ECCV)*, pages 3–19, 2018.
- [16] Y. Yang, Z. Nie, S. Huang, P. Lin, and J. Wu. Multilevel features convolutional neural network for multifocus image fusion. *IEEE Transactions on Computational Imaging*, 5(2):262–273, 2019.
- [17] A. Shakarami, M. B. Menhaj, A. Mahdavi-Hormat, and H. Tarrah. A fast and yet efficient yolov3 for blood cell detection. *Biomedical Signal Processing and Control*, 66:102495, 2021.
- [18] A. Dosovitskiy, L. Beyer, A. Kolesnikov, D. Weissenborn, X. Zhai, T. Unterthiner, and N. Houlsby. An image is worth 16x16 words: Transformers for image recognition at scale. *arXiv preprint arXiv:2010.11929*, 2020.
- [19] P. Alirezazadeh, M. Schirrmann, and F. Stolzenburg. Improving deep learning-based plant disease classification with attention mechanism. *Gesunde Pflanzen*, 75(1):49–59, 2023.
- [20] S. Wang, B. Z. Li, M. Khabsa, H. Fang, and H. Ma. Linformer: Self-attention with linear complexity. *arXiv preprint arXiv:2006.04768*, 2020.
- [21] R. J. Chen, M. Y. Lu, W. H. Weng, T. Y. Chen, D. F. K. Williamson, and F. Mahmood. Hierarchical vision transformers for medical image classification. *arXiv preprint arXiv:2203.10650*, 2022.
- [22] A. Shakarami, H. Tarrah, and A. Mahdavi-Hormat. A cad system for diagnosing alzheimer’s disease using 2d slices and an improved alexnet-svm method. *Optik*, 212:164237, 2020.
- [23] A. Shakarami, M. B. Menhaj, and H. Tarrah. Diagnosing covid-19 disease using an efficient cad system. *Optik*, 241:167199, 2021.
- [24] A. Shakarami, L. Nicole, and S. Ghidoni. Ai for advanced cancer diagnosis: a cad system empowered by a novel vision transformer network for histopathology analysis. *Virchows Archiv*, 485(S1):S397–S398, 2024.
- [25] M. Sandler, A. Howard, M. Zhu, A. Zhmoginov, and L. C. Chen. Mobilenetv2: Inverted residuals and linear bottlenecks. In *Proceedings of the IEEE Conference on Computer Vision and Pattern Recognition*, pages 4510–4520, 2018.
- [26] K. He, X. Zhang, S. Ren, and J. Sun. Deep residual learning for image recognition. In *Proceedings of the IEEE Conference on Computer Vision and Pattern Recognition*, pages 770–778, 2016.
- [27] O. Oktay, J. Schlemper, L. Le Folgoc, M. Lee, M. Heinrich, K. Misawa, and D. Rueckert. Attention u-net: Learning where to look for the pancreas. In *Medical Image Computing and Computer-Assisted Intervention – MICCAI 2018*, pages 358–366. Springer, 2018.
- [28] Zhong Zhang, Lixiang Liu, Yudong Zhang, and et al. Resunet++: An advanced architecture for medical image segmentation. *IEEE Access*, 8:110233–110241, 2020.
- [29] Yucheng Zhou, Fan Yang, Zhaohui Deng, Hongming Zhao, Ying Lu, and Lei Xing. H2g-net: Hybrid hierarchical graph network for cell segmentation in histopathological images. *Medical Image Analysis*, 75:102283, 2022.
- [30] Tao Wang, Han Liu, and Jian Zhang. Befunet: Boundary-enhanced feature fusion network for medical image segmentation. *IEEE Transactions on Biomedical Engineering*, 71(5):1534–1546, 2024.
- [31] L. Shen, W. Zhao, and L. Xing. Efficient deep learning-based organ segmentation using 3d

- patch-based learning and conditional random field. *Medical Physics*, 49(1):290–300, 2022.
- [32] S. Wang, Y. Zhu, L. Yu, H. Chen, H. Lin, and P. A. Heng. Annotation-efficient deep learning for automatic medical image segmentation. *Nature Communications*, 12(1):5915, 2021.
- [33] Mehdi Oquab, Thomas Darcet, Timothee Moutakanni, Huy Vo, Mateusz Szafraniec, Vitaliy Khalidov, and Piotr Bojanowski. Dino2: Learning robust visual features without supervision, 2023. <https://arxiv.org/abs/2304.07193>.
- [34] G. Litjens, P. Bándi, B. E. Bejnordi, O. Geessink, M. Balkenhol, P. Bult, and J. van der Laak. 1399 h&e-stained sentinel lymph node sections of breast cancer patients: the camelyon dataset. *GigaScience*, 7(6):giy065, 2018.
- [35] X. Wang, H. Tao, B. Wang, H. Jin, and Z. Li. Cfi-vit: A coarse-to-fine inference based vision transformer for gastric cancer subtype detection using pathological images. *Biomedical Signal Processing and Control*, 100:107160, 2025.
- [36] Shervin Minaee, Yuri Boykov, Fatih Porikli, Antonio Plaza, Nasser Kehtarnavaz, and Demetri Terzopoulos. Image segmentation using deep learning: A survey. *IEEE TPAMI*, 44(7):3523–3542, 2021.
- [37] Olaf Ronneberger, Philipp Fischer, and Thomas Brox. U-net: Convolutional networks for biomedical image segmentation. *MICCAI*, pages 234–241, 2015.
- [38] Jianpeng Chen, Yongyi Lu, Qihang Yu, et al. Transunet: Transformers make strong encoders for medical image segmentation. *Medical Image Analysis*, 67:101848, 2021.
- [39] H. Cao, Y. Wang, J. Chen, et al. Swin-unet: Unet-like pure transformer for medical image segmentation. *arXiv preprint arXiv:2105.05537*, 2021.
- [40] T. Wang, H. Liu, and J. Zhang. Befunet: Boundary-enhanced feature fusion network for medical image segmentation. *IEEE Transactions on Biomedical Engineering*, 71:1534–1546, 2024.
- [41] Shuo Sun, Wenqi Ren, Xinbo Gao, Rui Wang, and Xuequan Cao. Restoring images in adverse weather conditions via histogram transformer. *European Conference on Computer Vision*, Lecture Notes in Computer Science, LNCS 14561:111–129, 2024.
- [42] Jie Hu, Li Shen, and Gang Sun. Squeeze-and-excitation networks. *IEEE Transactions on Pattern Analysis and Machine Intelligence*, 42(8):2011–2023, 2020.
- [43] Sanghyun Woo, Jongchan Park, Joon-Young Lee, and In So Kweon. Cbam: Convolutional block attention module. *IEEE Transactions on Pattern Analysis and Machine Intelligence*, 42(10):2946–2955, 2020.

A Theorem

This section provides a theoretical foundation for the unit-based segmentation approach in UTS, where each tile of size $k \times k$ serves as the fundamental unit of prediction. The formulation addresses key challenges in histopathological image segmentation, namely label noise, computational complexity, and generalization in high-dimensional spaces.

Variance Reduction via Tile Aggregation. Let \mathcal{X} denote the space of WSIs, $\mathcal{Y} = \{1, \dots, C\}$ the label space, and $x_p \in \mathcal{X}_p$ a pixel from a WSI. In pixel-wise segmentation, a model $f: \mathcal{X}_p \rightarrow \mathcal{Y}$ may suffer from annotation noise, especially at decision boundaries or under staining variability. Let x_t be a tile containing k^2 pixels, then its label y_t is assigned via majority voting. The variance of the label noise is reduced as:

$$\mathbb{V}[y_t] \leq \frac{1}{k^2} \sum_{i=1}^{k^2} \mathbb{V}[y_i],$$

assuming independence across pixel labels. This makes tile-level predictions inherently more stable and less sensitive to noise compared to pixel-wise classification.

Multi-Level Feature Representation. Let ϕ_l, ϕ_m, ϕ_h denote features extracted at low, mid, and high abstraction levels within the encoder. MLFF module aggregates these as:

$$f_{\text{MLFF}} = \phi(\phi_l + \phi_m + \phi_h),$$

where $\phi(\cdot)$ is a nonlinear transformation. This can be interpreted as a residual composition over multiscale spaces. Theoretical results from function approximation show that multi-resolution architectures yield higher representational capacity: $\mathcal{F}_{\text{MLFF}} \supset \mathcal{F}_{\text{shallow}}$, enabling better convergence on complex tissue boundaries.

Attention Mechanisms as Input-Adaptive Kernels. Channel and spatial attention modules (DAT-SE and D-CBAM) act as dynamic filters. Given an input x , the attention-weighted output is:

$$f_{\text{att}}(x) = A(x) \odot f(x),$$

where $A(x)$ is an attention map and \odot denotes element-wise multiplication. This modulates feature activations conditioned on input statistics, mimicking adaptive kernel selection:

$$K_{\text{att}}(x, x') = \langle A(x)f(x), A(x')f(x') \rangle,$$

which improves class separation and supports context-dependent decision-making.

Bias–Variance Trade-off in High Dimensions. For the generalization error $\mathcal{E} = \text{Bias}^2 + \text{Variance} + \sigma^2$, where σ^2 denotes irreducible error, UTS reduces both bias and variance through architectural design:

- **Variance reduction** from tile aggregation and MLFF, - **Bias reduction** from attention-based adaptive modulation.

Thus, UTS improves learning efficiency in limited-label regimes and stabilizes optimization in high-dimensional feature spaces.

Complexity and Scalability. Pixel-wise models like U-Net have per-image complexity $\mathcal{O}(N \cdot K^2)$, where N is the number of pixels and K the kernel size. In contrast, unit-based segmentation performs $\mathcal{O}(M^2 \cdot D/k^2)$ operations for $M \times M$ token sequences and tile size k , yielding a significant speedup while preserving resolution-aware segmentation. This aligns with the practical need for scalable inference on gigapixel WSIs.

B Literature Review

Tissue segmentation in histopathological WSIs plays a central role in computational pathology, enabling high-throughput diagnostic support and quantitative tissue analysis [1, 36]. Traditional convolutional architectures such as U-Net [37] and DeepLab [5] perform dense pixel-wise segmentation, leveraging local receptive fields and spatial skip connections. Despite their effectiveness, these models are computationally intensive and demand densely annotated masks.

To address the limitations of locality and scalability, recent segmentation models have integrated transformers. Architectures like TransUNet [38], Swin-UNet [39], and H2G-Net [10] extend CNN backbones with self-attention to model long-range dependencies. Enhanced models such as BEFU-net [40] and HistoFormer [41] incorporate specialized modules for boundary enhancement and hierarchical context reasoning. Although effective in increasing spatial awareness, these models still rely on pixel-level granularity, which can introduce noise and hinder interpretability in clinical settings.

An emerging direction addresses the annotation bottleneck by shifting from pixel-wise to unit-based modeling, where each fixed-size tile is treated as a semantic entity. This design aligns with the diagnostic reasoning of pathologists, who often assess tissue in coherent regions rather than at the pixel level. Prior studies in weakly supervised learning and patch-level classification have laid the groundwork for this paradigm, but often lack structural consistency or systematic integration into segmentation pipelines.

Our work advances this research line by formalizing a unit-based framework, UTS, which segments WSIs at the tile level using a dedicated transformer backbone (UTS). Through multi-level feature fusion and adaptive attention mechanisms such as DAT-SE [42] and D-CBAM [43], the framework combines local morphology with global tissue context, providing a scalable and annotation-efficient solution for whole-slide histological analysis.